Evaluating the Utility of Pressure Scanners for Unsteady Pressure Measurements in Wind Tunnel Characterization of the Space Launch System

Pourya Nikoueeyan*, Michael D. Hind, John A. Strike, Marvin C. Perry, and Benjamin Wimpenny
Resono Pressure Systems Inc., Laramie, WY, 82072

Lee J. Mears[†], Patrick R. Shea[‡], Jesse G. Collins[§], Morgan A. Walker[¶], and Jeremy T. Pinier[‖]
NASA Langley Research Center, Hampton, VA, 23681

Jonathan W. Naughton**
University of Wyoming, Laramie, WY, 82071

In many aerodynamic measurement applications, the ability to make time-accurate measurements with pressure scanners provides practical advantages over making the same measurements directly using flush-mounted transducers. However, the pneumatic distortion due to the tubing between the sensing module and surface port limits the usefulness of such measurements to averaged, steady data only. This issue has restricted the application of pressure scanners for unsteady pressure measurements in the wind tunnel and flight-testing applications. The Wiener-filtered inverse system response model has been proven effective in reconstructing complex unsteady pressure signals acquired remotely using pressure scanners. The unparalleled long-term thermal stability, flexibility and robustness that pressure scanners provide in wind-tunnel and flight-testing applications, combined with an ability to reconstruct the unsteady components of the measured pressure signals, could enable their use in modern applications involving dynamic flow fields and highly separated flows. This work evaluated the feasibility of using pressure scanning systems for time-resolved pressure measurements in the NASA Langley 14- by 22-Foot Subsonic Wind Tunnel. Results demonstrated good agreement between the reference transducers and reconstructed pressure scanner measurements up to frequencies of approximately 500 Hz.

Nomenclature

A_c	Tubing cross-sectional area, in^2
c	Sonic velocity, ft/s
D	Tubing diameter, in
$G(\omega)$	Optimal filter function
h/L	Vehicle height over tower length
L	Length of tubing, in
M_∞	Freestream Mach number
N	Measurement noise estimate
p'	Mean-subtracted unsteady pressure, psi
$p_0(t)$	Surface pressure

---

*Chief Technology Officer, Resono Pressure Systems Inc., Member AIAA. ✉ nikoueeyan@resonopressuresystems.com

[†] Research Aerospace Engineer, Configuration Aerodynamics Branch, AIAA Member. ✉ lee.j.mears@nasa.gov

[‡] Research Aerospace Engineer, Configuration Aerodynamics Branch, AIAA Senior Member. ✉ patrick.r.shea@nasa.gov

[§] Research Aerospace Engineer, Configuration Aerodynamics Branch, AIAA Member. ✉ jesse.g.collins@nasa.gov

[¶] Research Aerospace Engineer, Configuration Aerodynamics Branch, AIAA Member. ✉ morgan.a.walker@nasa.gov

[‖] Research Aerospace Engineer, Configuration Aerodynamics Branch, AIAA Associate Fellow. ✉ jeremy.t.pinier@nasa.gov

**Professor, Mechanical Engineering Department, Associate Fellow AIAA. ✉ naughton@uwyo.edu

$P_0(\omega)$	Frequency-domain representation of $p_0(t)$
$\hat{p}_0(t)$	Deconvolved pressure from the transducer (estimate of surface pressure)
$\hat{P}_0(\omega)$	Deconvolved frequency-domain pressure from the transducer
$p_L(t)$	Sensed pressure at a transducer downstream of tubing
$P_L(\omega)$	Frequency-domain representation of $p_L(t)$
q_∞	Freestream dynamic pressure, psf
Re_D	Reynolds number based on core diameter
V	Transducer volume, in^3
ψ_{azm}	Azimuthal angle on model surface, degrees
ϕ	Phase lag, radians
ω	Circular frequency, radians
$\Upsilon(\omega)$	Frequency response function for $P_L(\gamma)/P_0(\gamma)$
Γ_P	Wave propagation factor
14x22	NASA Langley 14- by 22-Foot Subsonic Tunnel
A/D	Analog to digital
ASDF	Autospectral Density Function, psi^2/Hz
CFD	Computational Fluid Dynamics
ESP	Electronic pressure scanner
DTC	Digital Temperature Compensation
FRF	Frequency response function
ML-2	Mobile Launch tower for SLS Block 1B
PDF	Probability density function
SRB	Solid Rocket Booster
SLS	Space Launch System
SNR	Signal to Noise Ratio
WF-iSRM	Wiener-filtered inverse system model

I. Introduction

Robust and accurate measurement of unsteady surface pressures is essential for the characterization, modeling, prediction, and control of unsteady aerodynamics in the development of modern agile aircraft and space launch systems. Time-resolved unsteady pressure measurements at a large number of ports with high accuracy during wind tunnel and flight test applications provide insight and serve as validation data necessary for guiding Computational Fluid Dynamics (CFD) simulations. As opposed to direct load measurements, surface pressure data shed light on the localized flow physics that can better assist the CFD analysts in tuning the turbulence models and other crucial flow modeling parameters. However, acquiring unsteady pressure measurements robustly and accurately and in a time- and cost-effective fashion has been historically a challenging issue for instrumentation engineers.

Time-dependent unsteady pressure phenomena are currently measured using high-speed transducers located near to the point of measurement and are often flush-mounted to the surrounding surface. High-speed transducers capture frequencies in the tens of kilohertz ranges, but they are generally expensive and significantly increase the cost of high-spatial resolution measurements. Since they typically must be installed using adhesives, they cannot be conveniently replaced if damaged or reused in other measurement campaigns. Furthermore, when the local materials strain under load or temperature, the strain can be imparted to the pressure sensor and can lead to an unknown sensor bias that is difficult to remove from the pressure signal [1]. Even when there is minimal error owing to installation causes, there is generally a lower spatial resolution than for the tap/tubing/transducer pressure installations due to the cost, fragility, and greater installation complexity of high-speed transducers. It is also not uncommon to require two separate test articles for each transducer type (one instrumented with high-speed transducers and another one with tap/tubing installations) or to run two separate tests at the same conditions to capture the data separately. These problems can significantly increase the cost and time associated with tests that include unsteady pressure measurements compared to tests with only steady measurements.

Pressure scanners that contain many transducers per module (up to 64) are generally used to obtain higher spatial resolution but at a compromise of only steady-state (less than a few Hz and/or mean) measurements. For this type of measurement system, the transducer is placed remotely from the measurement location (the tap) and is connected to the transducer through a tubing system. The tubing provides isolation from heat, humidity, contamination, shock and physical contact. As a result, pressure scanners can be used reliably for long periods of time especially in harsh environments associated with high-speed wind tunnel testing [2, 3], flight [4, 5], field [6, 7], and track testing [8] applications. Pressure scanners are also easily transferable between test models and measurement campaigns, significantly reducing the cost of instrumentation for testing facilities.

However, hindering the use of pressure scanners for unsteady measurements is the connecting tubing that inherently introduces time lags and pneumatic distortion to the pressure signal received at the sensing element inside the pressure scanner. The character of the distortion varies and can be due to attenuation or resonant amplification depending on the geometry of the tubing, as well as the environmental conditions of the flow being measured [9, 10]. The pneumatic distortion (lag, attenuation and resonance) due to the tubing between the sensing module and surface port limits the usefulness of such measurements to averaged, steady data only. This issue has restricted the application of pressure scanners to steady measurements in the wind tunnel and flight-testing applications.

Modeling the physics of the tubing system provides a means by which to correct the signal distortions introduced by the tubing system. Derived from the conservation of mass, momentum, and energy, the model proposed by Bergh and Tijdeman [9] demonstrates good agreement with experimental data. However, due to the nature of the system response model, the higher frequency content of the signal, including any noise, gets amplified by a more significant amount in both amplitude and phase, compared to the low-frequency content, leading to inaccurate estimates of the surface pressure. Whitmore [11] improved this model by filtering the high-frequency content using a Wiener filter. This Wiener-filtered inverse system response model (WF-iSRM) has been proven to be effective in reconstructing complex unsteady pressure signals in a variety of low-speed wind tunnel testing applications [10, 12].

Through a collaborative effort between NASA, the University of Wyoming, and Resono Pressure Systems Inc., the feasibility of using pressure scanning systems for time-resolved pressure measurements in the NASA Langley 14- by 22-Foot Subsonic Tunnel (14x22) was evaluated. A 1.75%-scale model of the Space Launch System (SLS) Block 1B Cargo vehicle was selected for this evaluation effort. In particular, the liftoff configuration is considered where the launch vehicle is in proximity to the launch tower. The considerable flow separation typically encountered in this configuration [13] provides a unique opportunity for demonstrating the utility of this unsteady pressure measurement technique. Furthermore, the utility of pressure scanners [14] in providing surface pressure data for CFD validation purposes [15, 16] gives additional motivation to evaluate the effectiveness of this unsteady pressure reconstruction technique in further expanding the capabilities of pressure scanners. A recent NASA Technical Memorandum presents a detailed description of this experimental campaign [17].

This paper focuses on the methodology used for characterizing the effect of tubing lines and the unsteady pressure signal reconstruction technique. Different test cases with varying degrees of unsteady flow will be presented. The configuration of the ports and reference high-speed transducers allows for a side-by-side comparison of the performance of the reconstruction methodology utilized on measurements acquired using the pressure scanner with those of reference transducers. Different analytical tools will be used to evaluate the accuracy of the reconstructed unsteady pressure signals. The interaction between the launch vehicle and the launch tower exhibited a highly unsteady flow field with strong pressure fluctuations that were captured using the pressure measurement methodology described in this paper. A thorough assessment of the unique flow physics observed in this experimental campaign is described in a complementary paper [18].

II. Remote Sensing of Unsteady Pressure via Tap/Tubing Systems

This section provides the theory behind the tubing system response reconstruction, followed by a brief description of the instrumentation system and the methodology used for characterizing the tubing systems and reconstructing the pressure signals acquired during the wind tunnel measurements.

A. Theory

The response of a pressure transducer to an input pressure at the inlet of a length of tubing connected to the pressure transducer was first considered by Bergh and Tijdeman [9]. A typical configuration for a remotely mounted pressure transducer is depicted in Figure 1. The pressure $p_0(t)$ is the surface pressure and $p_L(t)$ is the sensed pressure at the transducer. The surface pressure is separated from the transducer by a length of tubing, L, with diameter, D, and transducer volume, V. The tubing length and transducer volume of this system result in signal attenuation or resonance and phase lag between the surface and measured pressures. Bergh and Tijdeman [9] derived a method to model the distortion based on the Navier-Stokes equations, equations of continuity and energy, and boundary conditions for the system of Figure 1. The result of this derivation is a frequency-domain transfer function (surface to sensor):

$$\frac{P_L(\omega)}{P_0(\omega)} = \Upsilon(\omega) = \left[\frac{1}{\cosh\left[\omega\Gamma_P \frac{L}{c}\right] + \frac{V\omega\Gamma_P}{A_c c}\sinh\left[\omega\Gamma_P \frac{L}{c}\right]}\right], \tag{1}$$

where $P_0(\omega)$ and $P_L(\omega)$ are the frequency domain representations of $p_0(t)$ and $p_L(t)$. ω is the circular frequency and Γ_P is the wave propagation factor described by Tijdeman [19] that specifies how the pressure varies as a function of frequency and longitudinal tube position. A_c is the cross-sectional area of the tube and c is sonic velocity of the gas.

Figure 2 demonstrates the typical frequency dependence of $\Upsilon(\omega)$ where, as expected, the attenuation and phase lag increase with frequency. The deconvolution of $P_L(\omega)$ with $\Upsilon(\omega)$ provides the estimated surface pressure, $\hat{P}_0(\omega)$. This deconvolution results in increased amplification of $P_L(\omega)$ with increasing frequency. When $\hat{P}_0(\omega)$ is transformed to the time domain, this signal amplification at high frequencies results in a noise dominated signal.

To control undesired signal amplification in the estimated surface pressure, an optimal filter, $G(\omega)$, is used in place of the simple deconvolution of Eq. (1)

$$\hat{P}_0(\omega) = G(\omega)\, P_L(\omega)\,. \tag{2}$$

The filter function $G(\omega)$ was developed by Whitmore and Wilson [11] to minimize the difference between actual and estimated surface pressures when noise is present on $p_L(t)$. This minimization results in

$$G(\omega) = \frac{\Upsilon^* \left(\frac{\|P_0\|^2}{\|N\|^2}\right)}{\|\Upsilon\|^2 \left(\frac{\|P_0\|^2}{\|N\|^2}\right) + 1}, \tag{3}$$

where $\left(\frac{\|P_0\|^2}{\|N\|^2}\right)$ is an approximation of the signal to noise ratio, SNR, and is the parameter used to tune the filter. As SNR decreases the amount of filtering increases. As SNR approaches infinity, $G(\omega)$ approaches $\Upsilon^{-1}(\omega)$ (inverse of Υ). The effect of SNR on the deconvolution is shown in Figure 3, where $G(\omega)$ tracks $\Upsilon^{-1}(\omega)$ to higher frequencies as SNR increases. Another feature of $G(\omega)$ is that its phase shift is not a function of SNR, such that while a lower SNR attenuates the deconvolved signal more, it does not introduce a phase lag. This derivation is similar to the optimal filter process developed by Norbert Wiener, and thus $G(\omega)$ is also referred to as the Wiener-filtered Bergh and Tijdeman transfer function. For brevity, this technique will be referred to as Wiener deconvolution throughout this paper. Further details on the derivation of this filter is provided by Whitmore and Wilson [11].

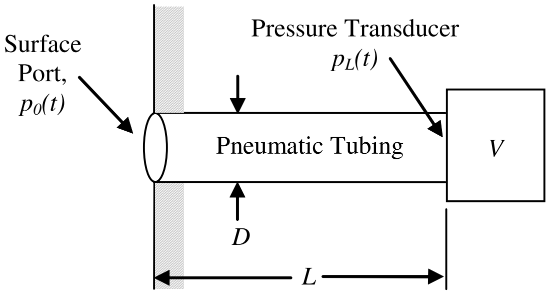

Fig. 1 Basic configuration of remotely mounted pressure transducer.

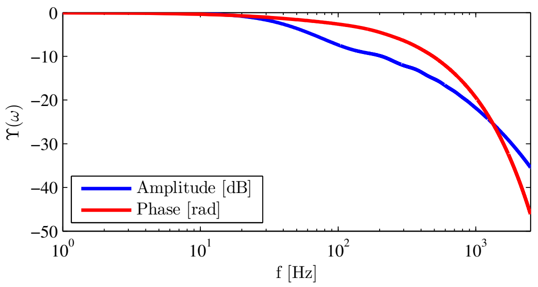

Fig. 2 Tubing system response transfer functions.

B. System Overview

Resono Pressure Systems' tubing response characterization and correction instrumentation system, utilized in this study, consists of two hardware components and a software package. The main hardware component is a data

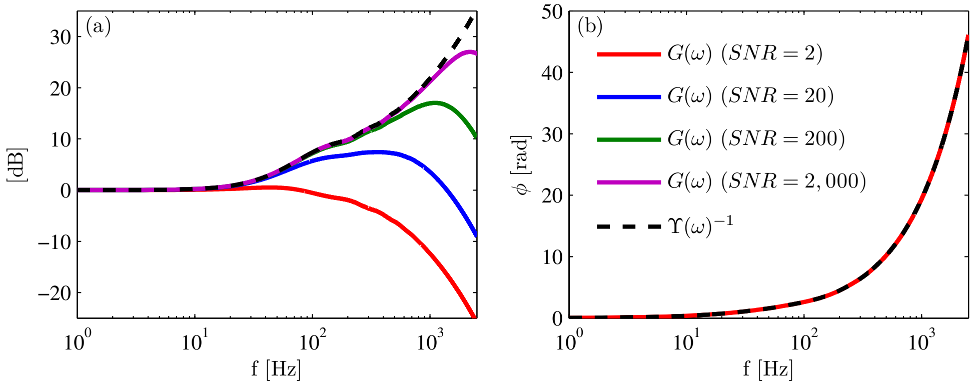

Fig. 3 Filtered tubing system response transfer functions.

acquisition and instrument control system that allows time-accurate interfacing with pressure scanners. High-speed digital addressing and Analog-to-Digital (A/D) conversion are needed to ensure that the unsteady pressure signals acquired using the pressure scanners have the necessary temporal resolution for further signal processing and application of the Wiener deconvolution. In addition to the data system, an in situ tubing response characterization device (shown in Figure 4 (a)) is utilized that allows for characterizing the dynamic response of any tap-tubing-transducer system. The in situ characterization enables extracting the necessary data required for optimizing the parameters (tubing geometry and filtering parameters) used in the Wiener deconvolution of the signals acquired using the characterized pressure channel. The software package processes the pressure measurements and tunes the Wiener deconvolution parameters. In addition, methods to quantify uncertainties associated with the measurement and correction of the distorted signals are in development.

Once the model has been installed in the test section, the in situ tubing response characterization is performed on each pressure tap. The nominal tubing geometry for the pressure tap/tubing under characterization and the data acquired from the hand-held device are then used to optimize the Wiener deconvolution parameters. The wind tunnel runs can occur before or after the in situ characterization step. However, performing this step before testing can determine any leaking or blockage in the tubing systems. The optimized Wiener deconvolution parameters extracted after the in situ characterization are then used to reconstruct any remotely-measured pressure signal acquired using the pressure scanner. The parameters can be reused as long as the tubing geometry of the individual pressure taps stays the same.

C. In situ Tubing System Response Characterization

As mentioned previously, prior to the wind tunnel runs, the dynamic response of each length of tubing routed to a port on the pressure scanner is characterized via the in situ tubing response characterization device. This device utilizes a fast-acting pneumatic valve. The valve generates a pressure pulse that is measured locally, p_0, and provided as input to the tubing system. The pressure signal measured by the pressure scanner module is the output of the tubing system, p_L. The scanner measurement, p_L, and applied pressure, p_0, are sampled simultaneously at 10 kHz during this process. The data acquired in this process are then used to evaluate the dynamic response of the tubing system and tune the theoretical model $G(\omega)$ that describes the dynamic response of each pneumatic line. For each pneumatic line, the reconstructed pressure signal, $\hat{p}_0$, that results from applying Wiener deconvolution to the p_L signal is compared against the reference signal, p_0. The parameters are tuned such that the application of the Wiener filter can restore as much of the frequency content as possible. Once the desired agreement between $\hat{p}_0$ and p_0 is achieved (in time and frequency domains), the tubing system parameters are stored to process the data acquired during the wind tunnel runs.

Data acquired during the tubing response characterization of a representative port are shown in Figure 4 (b) to showcase the typical response of the tubing runs used in the test article studied in this work. The time-domain plot shows a short (2 ms) pressure impulse generated using the fast-acting valve as a solid black line. For the tubing system considered here, the remote pressure signal measured with the scanner module and plotted in solid red, p_L, exhibits significant attenuation and time lag compared to the reference pressure p_0. Performing Wiener deconvolution aims to address such distortions in the p_L signal. It is clear that the reconstructed signal, $\hat{p}_0$, shown with a dashed blue

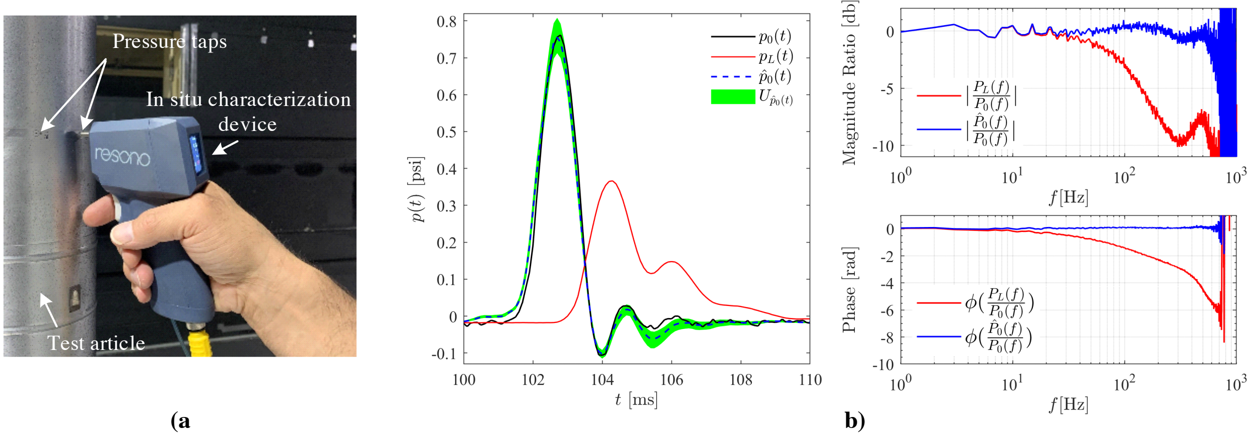

(a

b)

Fig. 4 (a) The in situ tubing characterization device is used to evaluate the dynamic response of each pressure tap/tubing system. (b) Time and frequency-domain response of the tubing system associated with a representative port on the test article. p_0 is the input to the tubing system and p_L is the signal measured with the pressure scanner; $\hat{p}_0$ is the result of utilizing the Wiener deconvolution to reconstruct the distorted signal.

line, recovers much of the attenuated and delayed content and better represents the reference transducer signal p_0. This is further evident by examining the amplitude ratio and phase for the transfer functions calculated using both raw and reconstructed signals with respect to the reference transducer. Clearly, the mechanical response of the valve limits the maximum frequency content in the generated impulse, which is near 400 Hz for the current configuration. Consequently, the noise observed in the magnitude ratio plot above 400 Hz is due to the absence of appreciable pressure signal content. The uncertainty in the reconstructed signals is also shown for the time-domain representation. The uncertainty band shown in Figure 4 (b) is estimated based on assuming a 5% input uncertainty across all variables used in the Wiener deconvolution. For the most part, the reference transducer signal lies within the uncertainty band around the reconstructed signal except for the slight deviation observed for the initial rising edge of the signal.

D. Reconstruction of Unsteady Pressure Measurements Acquired During Wind Tunnel Tests

Wind tunnel measurements are conducted after performing the in situ characterization. Resono Pressure Systems' data acquisition system is used to acquire unsteady pressure data during the wind tunnel runs. Raw pressure scanner measurements are recorded during each run and after the completion of the wind tunnel runs, scanner measurements are processed to address the tubing effects. In this step, the software processes each channel individually using the Wiener deconvolution parameters stored for that channel. Figure 5 showcases the results of the reconstruction applied to measurements acquired during a representative test run. The raw pressure signal acquired from a pressure tap on the test article and routed to the scanner module is plotted in solid red, p_L, and exhibits considerable temporal lag and attenuation of higher frequency fluctuations compared to the simultaneously acquired reference pressure transducer signal p_0 plotted in solid black. The result of applying the Wiener deconvolution to the scanner signal $\hat{p}_0$ is shown with a dashed blue line. The software applies a similar process to all pressure scanner ports and the reconstructed unsteady pressure signals are then stored for post-processing purposes.

Further description of the experimental setup and the instrumentation used to acquire the signals shown in Figure 5 is provided in the next section followed by an in-depth analysis of the outcome of the reconstruction methodology in the Results section.

III. Experimental Setup

This section presents the experimental facility and the test article. The reference unsteady pressure measurement instrumentation used for comparison against reconstructed measurements is also described here. At the end of this section, the test cases included in this paper are highlighted.

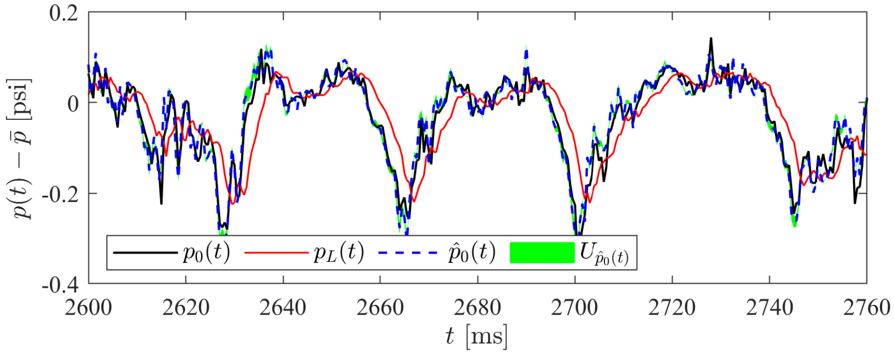

Fig. 5 Pressure records acquired during a representative wind tunnel run. p_L is the signal measured with the pressure scanner; $\hat{p}_0$ is the result of utilizing the Wiener deconvolution to reconstruct the distorted signal, and p_0 is the signal acquired using a flush-mount high-speed transducer.

A. Wind Tunnel Facility and Test Article

The experimental facility utilized in this work was the NASA Langley Research Center 14- by 22-Foot Subsonic Tunnel (14x22). As described by Gentry et al. [20], this atmospheric, closed-circuit, low-speed wind tunnel facility allows for a wide range of testing conditions and test-section configurations. Due to the relatively small size of the test model, the test-section configuration during this experiment was with closed walls [14]. With the walls closed, the test section dimensions are 14.5 ft high by 21.75 ft wide by 50 ft long.

The wind tunnel model was a 1.75% scale model of the Space Launch System (SLS) Block 1B Cargo vehicle installed next to a scale model of a Mobile Launch platform (ML-2). The wind tunnel model is shown in Figure 6 (a). Distributed roughness (#80 grit carborundum) is applied to the entire launch vehicle surface to promote transition; however, the roughness effect on the flow around this test article has not been verified. The gap between the launch vehicle and the closest face of the ML-2 is approximately 1.28 core diameters. This instrumentation effort focuses on a single azimuthal array of pressure taps on the vehicle center body away from the solid rocket boosters (SRBs); the approximate location of this array is shown with a blue band in Figure 6 (a). For further information regarding the test article and the wide range of testing configurations and test cases considered in this experimental effort, the reader should consult Mears et al. [17].

B. Instrumentation

The instrumented test article was the cargo nose of the 1.75% scale model of the SLS Block 1B Cargo vehicle. The test article was equipped with a pressure scanner module and five flush-mounted high-speed pressure transducers. Twelve pressure taps were placed around the test article, and each was routed to the pressure scanner via approximately 14 inches of stainless-steel and vinyl tubing. At five locations, a high-speed pressure transducer was also mounted next to the pressure taps to provide a high-speed reference measurement. This arrangement is shown in Figure 6 (b). The configuration of the pressure taps, and high-speed transducers on the test article allow for side-by-side comparison of the reconstructed remotely-measured pressure signals with that of a flush-mounted high-speed transducer.

1. Pressure Scanner Module

The pressure scanner used in this work is a DTC ESP-32HD with a full-scale range of 1 psi developed by TE Connectivity (PSI). The pressure scanner module benefits from the proprietary Digital Temperature Compensation (DTC) technology. Each pressure scanner module is factory calibrated to compensate for nonlinearity and temperature errors resulting in highly accurate measurements with minimal thermal sensitivity. It is important to note that Pressure scanner modules do not sample individual channels simultaneously; instead, the output pressure (and temperature) signal is multiplexed. Due to the multiplexed structure of the output signal, pressure measurements cannot be analog filtered with antialiasing filters. Mears et al. [17] discuss the potential effects of aliasing on scanner measurements.

The tubing length between the twelve pressure taps and the ESP scanner was approximately 14 inches total, comprised of 6 inches of stainless steel tubing, 8 inches of 0.040-inch diameter Tygon tubing, and an adapter with short

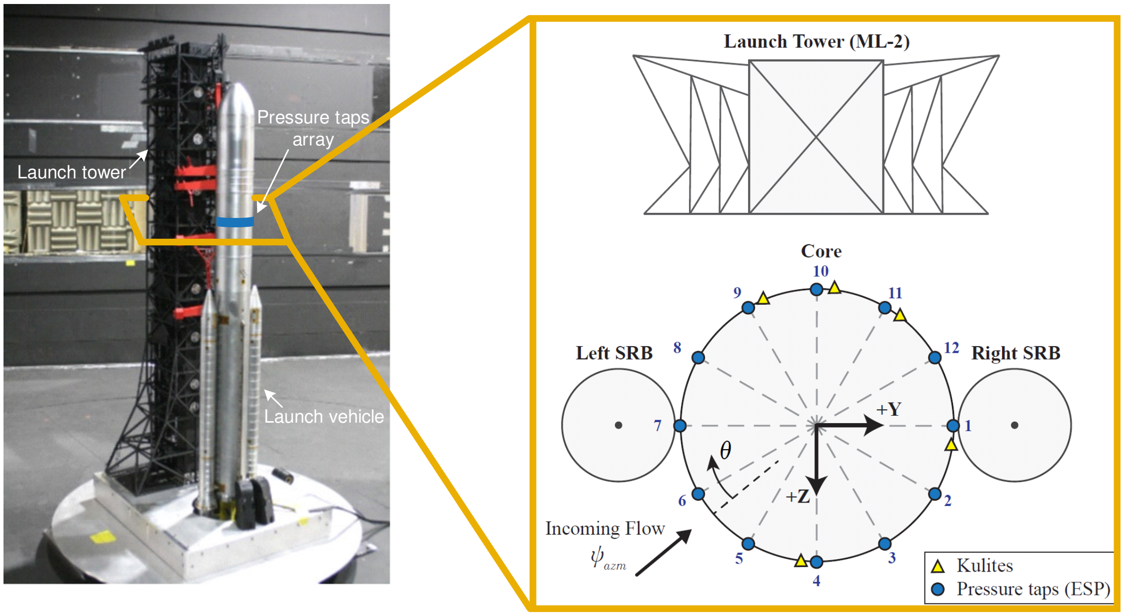

(a) **(b)**

Fig. 6 (a) SLS Block 1B Cargo 1.75% scale model with mobile launch tower (not to scale) installed in the closed test section of the Langley 14 × 22 wind tunnel. (b) Top-down view of the model showing the location of 12 pressure taps and 5 surface-mounted Kulites spaced 3° from the taps.

lengths of 0.065-inch diameter tubing to connect to the ESP module. Such complex tubing systems with multiple tube cascades could significantly influence the dynamics of the pressure propagation in the line compared to the same length of uniform tubing. The tubing system response model [9] utilized here accounts for cascaded systems. Despite the similar nominal geometry of all twelve ports, the in situ tubing characterization process, discussed in section II.C, was performed on all twelve ports to account for any deviation in the nominal geometries.

The pressure scanner module was connected to the facility calibration system. Five-point static calibrations were performed before the model build-up to update the offset and span of the scanner calibration routines. After model installation, the module was inadvertently connected to a separate calibration line with a leak. Consequently, periodic static calibration of the pressure scanner module was not possible until a later phase of testing when this line could be accessed. All pressure channels demonstrated highly stable sensitivity values, and the highest deviation in sensitivity among three different calibrations was less than 0.4%.

2. *Reference Pressure Transducers*

Five surface-mounted, piezoresistive pressure transducers are used to provide validation data for the unsteady pressure measurements acquired remotely using the pressure scanner module. The reference transducers were placed close to the static pressure taps to provide a validated pressure reading at Ports 1, 4, 9, 10, and 11 (Figure 6 (b)), and the transducers were installed 3° azimuthally away from corresponding pressure taps. Ports 1 and 4 were instrumented with XCL-19-IA-072 transducers manufactured by Kulite® Semiconductor Products, while Ports 9, 10, and 11 were instrumented with XCL-31-IA-072 transducers, also manufactured by Kulite®. The 15 psi differential pressure transducers were preamplified to provide a nominal static sensitivity of 165 mV/psi. This pressure range was much higher than required for this test, since the peak pressure fluctuations observed in this effort were on the order of 0.2 psi, or 33 mV. The relatively low sensitivity was not desirable, and instrument noise became a significant concern during testing [17]. The noise signature also differed between the XCL-19 (Ports 1 and 4) and XCL-31 (Ports 9-11) Kulite®s due to differences in the in-line amplifiers, resulting in instrumentation noise obscuring the lowest pressure fluctuations measured.

The high-speed transducers were calibrated by applying a range of known pressures to the common reference line and recording the output voltage through the data acquisition system. Because the reference line was shared with other facility equipment, the transducers were calibrated over the range of 0.16 psi. Although the calibrated range is lower than the full range of the sensors, the majority of test conditions did not exceed the calibration bounds. A linear regression was then applied to the measurements to calculate the offset and sensitivity for each transducer.

3. Signal Acquisition and Synchronization

Data acquisition was conducted using Resono's data acquisition and instrument control system. As described previously, twelve pressure taps on the scanner module were used. Each subsequent port on the scanner module is sampled at $40\mu s$ intervals within a $500\mu s$ scan. This translates to a per-port sampling frequency of 2000 Hz when all twelve channels are continuously scanned. Two 4-channel National Instruments NI-9239 high-speed voltage acquisition cards simultaneously acquired pressure signals from five Kulite® validation transducers. The Kulite® transducers' outputs were recorded at 50 kHz. The NI-9239 modules apply sigma-delta antialiasing filters with a cutoff frequency of 22.5 kHz. This introduces an additional time delay in the signals acquired using the NI-9239 modules. All data acquisition channels (scanner and reference transducers) are synchronized and time-stamped using NI Sync drivers with submicrosecond accuracy. This allowed for aligning the data streams and correcting the delays associated with the antialiasing filter in data post-processing prior to performing any analysis on the measurements [17].

The high-speed transducers were sampled at a significantly higher rate than that of the pressure scanner modules. To allow for a side-by-side comparison of the signals in the time and frequency domain, the signals acquired using the high-speed transducers were decimated to match the sampling rate of the pressure scanner's ports. Decimation reduces the sampling frequency to a lower rate. However, a lowpass filter is commonly applied to the signal to avoid aliasing. MATLAB® function `decimate` with a third-order Chebyshev filter was utilized for the analysis presented in this paper. The result of the decimation is compared against the original validation transducer signal for a representative test case in Figure 7. Time-domain comparison (Fig. 7(a)) shows a good overall agreement between the two signals. It also indicates that the phase of the decimated signal is preserved compared to the original signal. The probability distributions (Fig. 7(b)) display a similar statistical distribution between the the two signals. The Autospectral distribution of the decimated signal is compared against that of the original signal in Figure 7(c). The decimation produces an equivalent spectral distribution for the decimated signal up to 940 Hz. Only a slight deviation in the energy of the two signals is observed at frequencies close to 1000 Hz, which is due to the imposed filtering effects. Overall, decimation produces results that represent the original signals and can be used to validate the reconstructed scanner measurements.

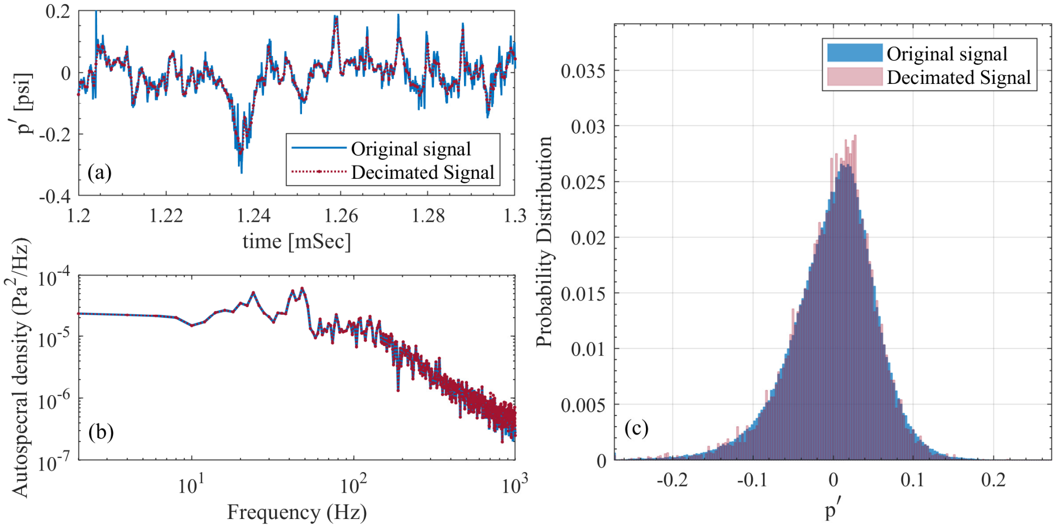

Fig. 7 Comparison between the original reference transducer signal and the decimated signal for a representative test case.

C. Test Cases and Conditions

During the experimental campaign, three testing sequences were conducted, each consisting of similar flow conditions with changes to the model configuration. Mears et al. [17] provide a detailed description of the testing configurations and conditions. Only three test cases are selected from a single test sequence to be discussed in this paper. During this sequence, the Mobile Launch tower was present next to the launch vehicle, and the support umbilicals were retracted away from the vehicle to emulate the liftoff configuration as it was shown in Figure 6 (a). The model is mounted on a sting with motorized height adjustment relative to the launch tower. Tests were conducted at different height-to-tower ratios h/L where h equals the vertical elevation of the vehicle above the launch platform, and L is the height of the launch tower. Due to the selected reference point on the vehicle, h/L = -0.003 is the lowest height tested, where the launch vehicle sits at the ground plane prior to liftoff. The vehicle and launch tower are mounted on a yaw table perpendicular to the wind tunnel floor in the liftoff configuration. In this configuration, the vehicle's angle of attack is 90°, and the freestream flow simulates incoming ground winds. Tests were conducted at different incoming wind directions ψ_{azm} measured clockwise. The definition of the wind direction is shown in Figure 6(b); at ψ_{azm} = 0° the vehicle is behind the tower with respect to the incoming flow. Temperature variations resulted in a range of Mach and Reynolds numbers during testing. For nominal dynamic pressure (q_∞) equal to 50 psf, the Mach number varied between 0.1846 and 0.1871. The dynamic pressure typically varies by 0.3% during data acquisition. Variations in outdoor temperature resulted in test section temperatures from 70°F to 108°F, with unit Reynolds number ranging from 1.2 to 1.3 $\times 10^7$/foot ($Re_D = 5.3 \times 10^5$ to 6.0×10^5). Here, a short overview of the testing conditions for each selected test case is provided; These conditions are summarized in Table 2.

1) Case 1: This case highlights the conditions where the launch vehicle sits at the ground plane (h/L = -0.003) and the incoming flow angle is ψ_{azm} = 180°. In this case, the tower is located directly downstream of the launch vehicle. Under these conditions, the azimuthal array of pressure taps can pick up the wake interaction between the vehicle and tower.
2) Case 2: This case highlights the conditions after the liftoff where the h/L = 0.299 and the incoming flow angle considered is ψ_{azm} = 350°. In this case, the tower is upstream of the vehicle. At the selected combination of height and flow angle, the shear layer produced by the flow over the top of the tower impinges near the axial location of the pressure sensors.
3) Case 3: This case highlights the conditions where the vehicle is nearly clear of the launch tower at h/L = 0.876 (and the pressure port array is far outside direct influence of the tower). The flow angle considered here is ψ_{azm} = 240°.

These test cases have been selected to allow for evaluating the quality of the reconstruction methodology across a wide range of conditions. For a detailed discussion of the flow physics observed in this wind tunnel test, the reader should refer to Mears et al. [18].

Table 2 Summary of test cases discussed in this paper

	h/L	ψ_{azm} [°]	q_∞ [psf]	M_∞
Case 1:	-0.003	180	50	0.186
Case 2:	0.299	350	50	0.186
Case 3:	0.876	240	50	0.187

IV. Results and Discussion

In the presence of the launch tower, the flow around the forebody shroud of the SLS Block 1B Cargo variant results in an unsteady pressure field that provides an exceptional validation opportunity for the pressure signal reconstruction methodology discussed in this work. This paper examines three different test cases with highly dynamic surface pressure signatures. These cases have been selected to highlight different aspects of the rich flow physics experienced in this experimental campaign. First, the time-domain signals from remote and surface transducers are compared to qualitatively demonstrate the efficacy of the signal reconstruction. Statistical and spectral representations are presented next to provide a more detailed comparison between the reconstructed scanner signal with that of the reference transducer. Data from three port locations are presented throughout the result sections for brevity. Ports 9, 10, and 11 have been selected for this purpose. Besides having neighboring high-speed validation transducers, their proximity to one another allows one to evaluate the results across multiple ports for each test case under consideration. Note that reaching a perfect correlation between the reconstructed and high-speed transducer measurements is not feasible due to the slight spatial difference between the two sensor locations.

A. Time-domain Analysis

The time-domain representation allows for visual assessment of the challenges associated with capturing the unsteady content of the pressure data acquired remotely using pressure scanners. Figures 8, 9, and 10 present the results for three neighboring pressure taps and their associated reference transducers for the three test cases considered in this work. Each plot displays a time recording of the measured pressure fluctuations on the test article at one location. Note that the y-axis scales have been adjusted for each figure to highlight the quality of pressure reconstruction.

The first case (Figures 8) represents a scenario with relatively high-amplitude fluctuations with indications of strong periodicity in the time domain signals. The second case (Figure 9) exhibits high-frequency fluctuations with lower amplitudes, and the third case (Figures 10) presents the weakest unsteadiness observed among the cases considered here. Close inspection of the $p_0(t)$ and $p_L(t)$ signals for all three cases indicate that the remotely acquired signals follow the reference signal with significantly reduced amplitude and phase lag. This is due to the low-pass filtering effect that the tubing system imposes on the pressure signals propagating through it. Applying the Wiener deconvolution results in reconstructed signals ($\hat{p}_0(t)$) that demonstrate a significantly improved agreement in both amplitude and phase with those of their associated reference transducer. Furthermore, it should be noted that for cases with higher-amplitude fluctuations and hence a stronger signal-to-noise ratio, the quality of the reconstruction improves inherently. As a result, it should be noted that the quality of the comparison is mainly dependent on local flow conditions and the associated instrumentation noise. This will be discussed in more detail in the frequency domain analysis. After evaluating the time-domain signals, the reasonable agreement observed here provides further motivation for a more detailed analysis.

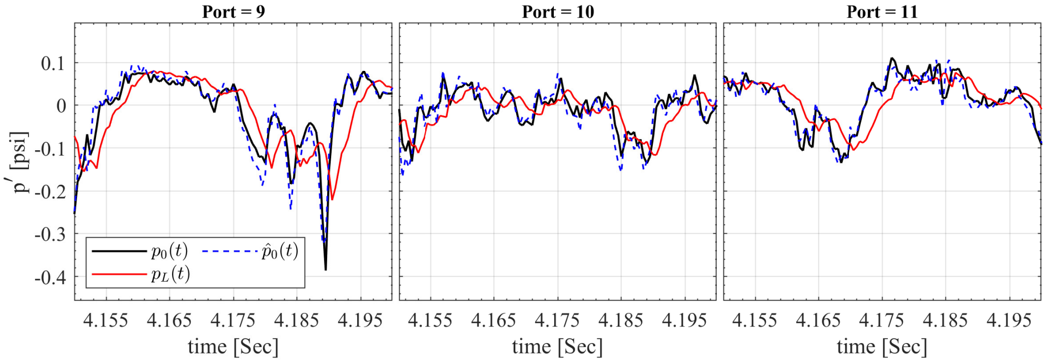

Fig. 8 Time-domain comparison between pressure fluctuations for the measured ($p_L(t)$ and $p_0(t)$) and reconstructed $\hat{p}_0(t)$ signals | Case 1: q_∞ = 50 psf, h/L = -0.003, and ψ_{azm} = 180°.

B. Statistical Analysis

As seen in time-domain representations, the filtering effect imposed by the tubing system reduces the amplitude of the pressure fluctuations. The statistical characteristics of the pressure fluctuations can be used to assess the efficacy of

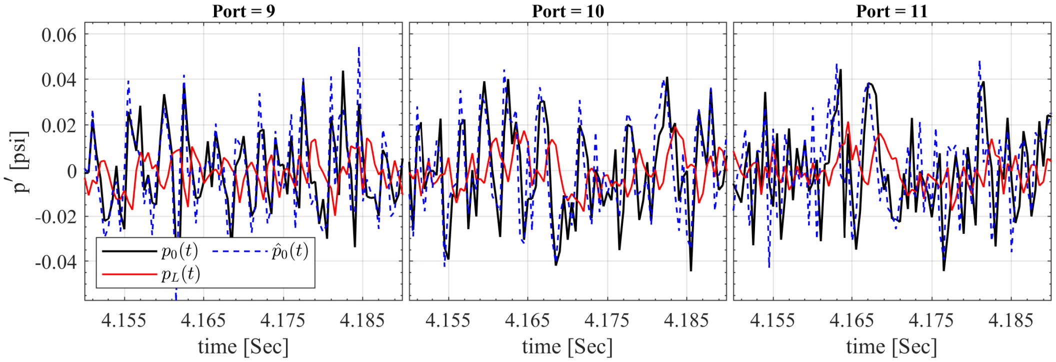

Fig. 9 Time-domain comparison between pressure fluctuations for the measured ($p_L(t)$ and $p_0(t)$) and reconstructed $\hat{p}_0(t)$ signals | Case 2: q_∞ = 50 psf, h/L = 0.299, and ψ_{azm} = 350°.

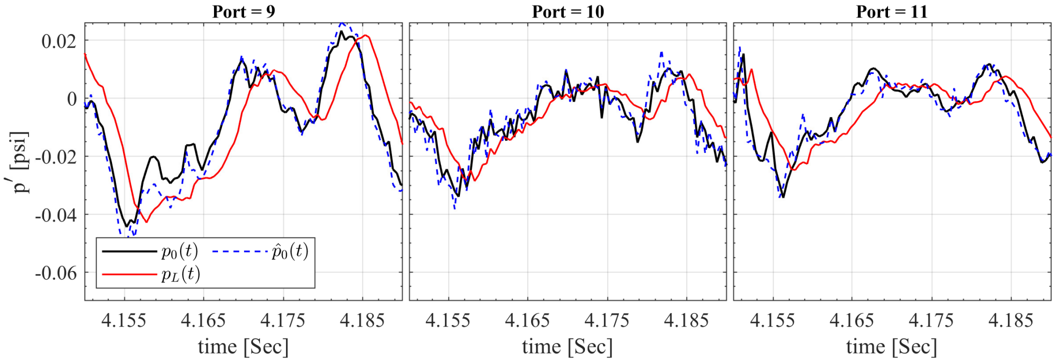

Fig. 10 Time-domain comparison between pressure fluctuations for the measured ($p_L(t)$ and $p_0(t)$) and reconstructed $\hat{p}_0(t)$ signals | Case 3: q_∞ = 50 psf, h/L = 0.876, and ψ_{azm} = 240°.

the Wiener deconvolution in reconstructing the attenuation in the remote measurements. The probability distributions for $p_0(t)$, $p_L(t)$ and the reconstructed $\hat{p}_0(t)$ serve as a reasonable basis for comparing the overall behavior in one long record. Figures 11, 12, and 13 present the probability distribution functions (PDFs) for three neighboring pressure taps and their associated reference transducers for the three test cases considered in this work. Except for the first test case, where the tower is located directly downstream of the launch vehicle, all other distributions presented here exhibit symmetric and approximately Gaussian behaviors. Regardless of the shape of the distribution, which is influenced by the local flow state, similar trends can be attributed to the tubing effects.

Clearly, the attenuation in the amplitude of the raw pressure scanner signal $p_L(t)$ exhibits reduced peak-to-peak fluctuations resulting in a taller peak and narrower distribution with relatively shorter tail, and as a result smaller standard deviation σ compared to that of the reference transducer signal $p_0(t)$. This is particularly evident for the second case (Figure 12) where the higher frequencies and lower amplitudes, observed in the time domain signals, suffer more aggressively from the attenuation imposed by the tubing. The tails of the distribution for the raw scanner signal carry significantly less weight for all three ports shown in Figure 12. Once the Wiener deconvolution is applied to the data and the pressure signal is reconstructed, a significantly improved agreement between the reconstructed and reference transducer distributions is achieved.

The last test case shown in Figure 13 showcases an important characteristic of the tubing system response behavior. This case exhibited sluggish time signals (Figure 10) that suggest less spectral energy at higher frequencies. This helps with preserving the amplitude of the pressure fluctuations as they propagate through the tubing system. As a result, sample distributions are less influenced by amplitude distortions. For such signals, the primary cause of the distortion is attributed to the time lag associated with the wave propagation in the pneumatic tubing between the surface and the sensing element inside the pressure scanner module.

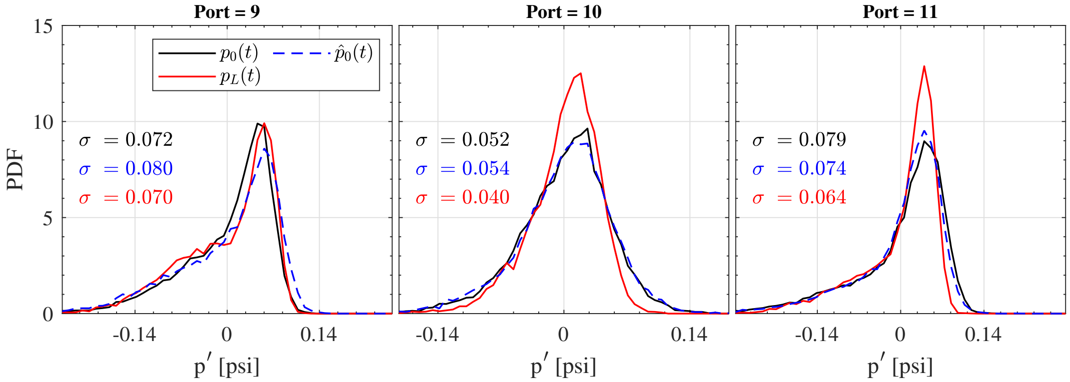

Fig. 11 PDFs for the measurements acquired from the reference transducers, the raw scanner measurements, and the reconstructed scanner signals | Case 1: q_∞ = 50 psf, h/L = -0.003, and ψ_{azm} = 180°.

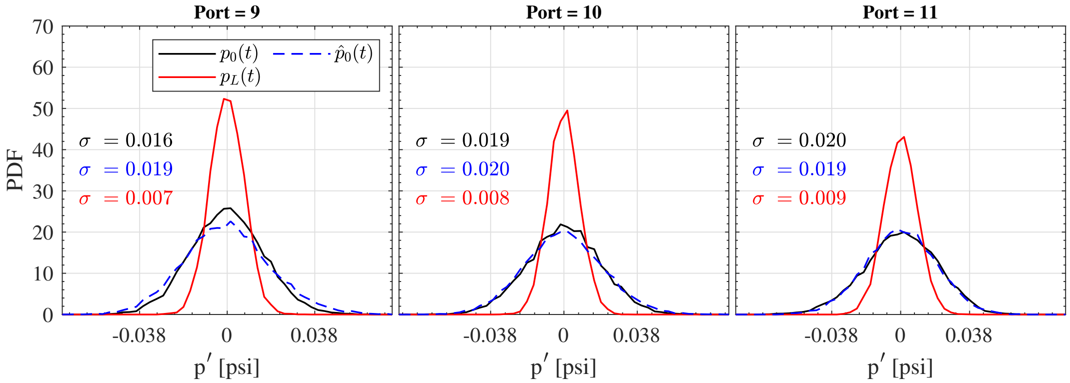

Fig. 12 PDFs for the measurements acquired from the reference transducers, the raw scanner measurements, and the reconstructed scanner signals | Case 2: q_∞ = 50 psf, h/L = 0.299, and ψ_{azm} = 350°.

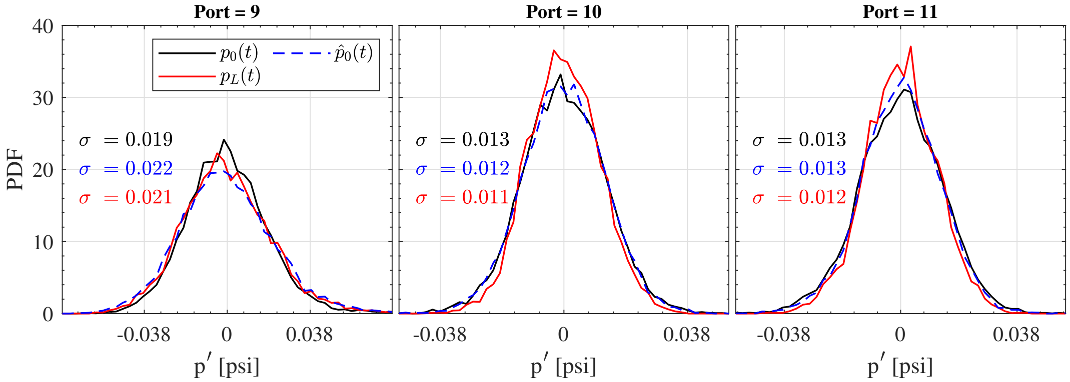

Fig. 13 PDFs for the measurements acquired from the reference transducers, the raw scanner measurements, and the reconstructed scanner signals | Case 3: q_∞ = 50 psf, h/L = 0.876, and ψ_{azm} = 240°.

C. Frequency-domain Analysis

Spectral analysis of the pressure signals before and after applying the Wiener deconvolution is also of great interest. Such analysis provides a basis for evaluating the efficacy of the reconstruction over a wide range of frequencies. Here, the Autospectral density function (ASDF) is used to assess the signals in the frequency domain. Typical spectra for ESP measurements and decimated reference transducer signals are calculated using Welch's periodogram method with averaging block sizes of 1000 samples, resulting in frequency resolution of 4 Hz and a total number of 12 averages with Hamming windowing.

Figures 14, 15, and 16 present the ASDFs associated with the reference transducer signal, $p_0(t)$, along with those of the raw, $p_L(t)$, and reconstructed, $\hat{p}_0(t)$, signals acquired using the pressure scanner module for the three test cases considered in this paper. The ASDFs associated with the reference transducers and raw scanner measurements indicate a fairly good agreement up to 70 Hz across all cases. Above this frequency, the low-pass filtering effect caused by the tubing significantly attenuates the amplitude of the ASDFs calculated using raw pressure scanner measurements. It is important to point out that in most cases, the dominant frequencies and well-defined peaks in each spectra are still easily detectable in the ASDF of the raw scanner signal even though the spectrum's amplitude is significantly smaller than that of the reference transducer. After applying the Wiener deconvolution to the $p_L(t)$ signals, the resulting $\hat{p}_0(t)$ spectra indicate significantly better agreement with reference transducers. The ASDFs for the first test case with the highest pressure fluctuations at h/L = -0.003, and ψ_{azm} = 180° are shown in Figure 14. The three sensors near the tower all show reasonably good agreement between the reconstructed and reference transducers up to nearly 700 Hz, where the reconstructed signals show higher energy than measured by the reference transducers. Similar trends were observed in other test cases, including cases 2 and 3 presented here. There is no physical cause that would be expected to produce this shift, and it is reasonable to attribute this behavior to aliasing present in the scanner signal [17]. The potential sources of these features are still under investigation. It is important to note that good agreement between the reconstructed and reference transducer signals was achieved in all three test cases. However, the range of frequencies

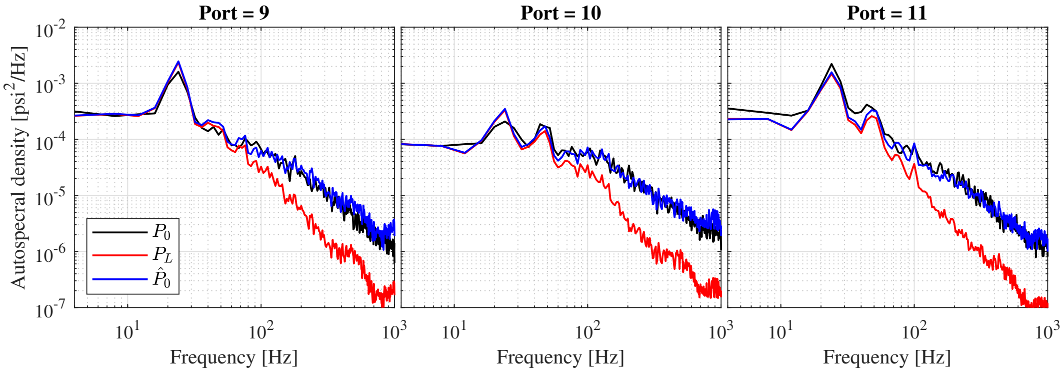

Fig. 14 Autospectral density functions for the measured signals (pressure scanner and high-speed transducer) and the reconstructed signal | Case 1: q_∞ = 50 psf, h/L = -0.003, and ψ_{azm} = 180°.

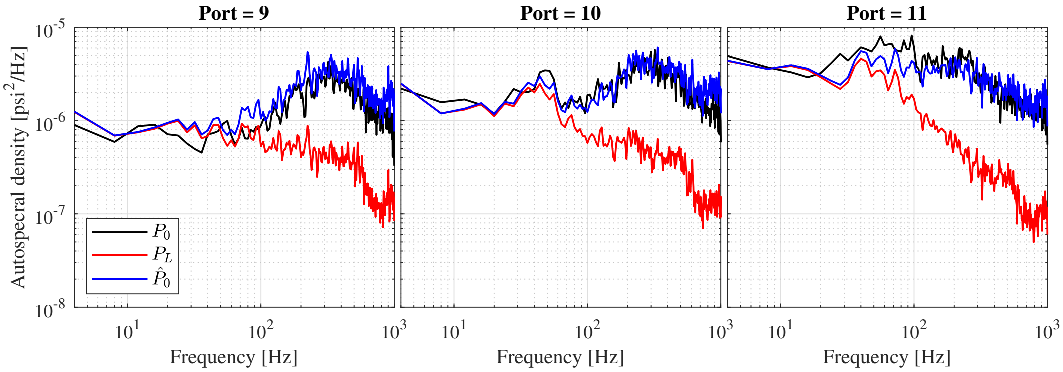

Fig. 15 Autospectral density functions for the measured signals (pressure scanner and high-speed transducer) and the reconstructed signal | Case 2: q_∞ = 50 psf, h/L = 0.299, and ψ_{azm} = 350°.

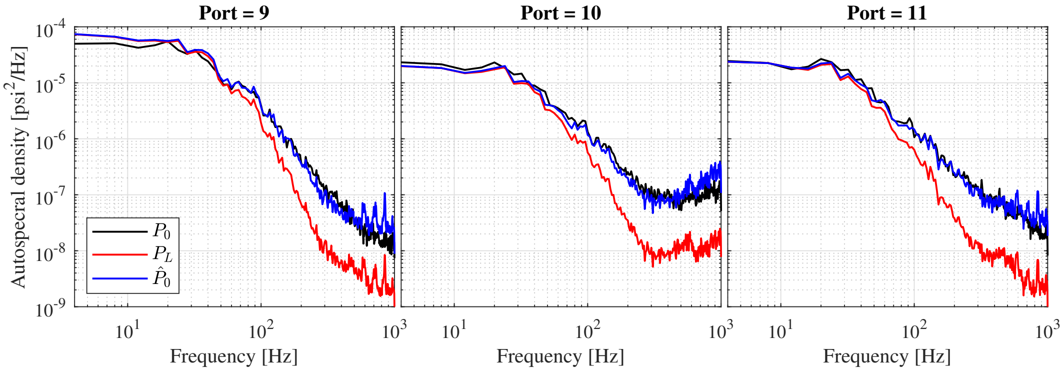

Fig. 16 Autospectral density functions for the measured signals (pressure scanner and high-speed transducer) and the reconstructed signal | Case 3: q_∞ = 50 psf, h/L = 0.876, and ψ_{azm} = 240°.

with a strong agreement between the two ASDFs can vary significantly depending on the signal-to-noise ratio for the scanner signal. The Wiener deconvolution amplifies the energy at lower frequencies and suppresses the higher frequency content. As a result, in cases with strong signal content and, as a result, a strong signal-to-noise ratio, a better agreement between the reconstructed and reference signals was achieved.

D. Fluctuating Pressure Intensity Distribution

The benefit of employing the pressure reconstruction approach discussed here is that it can be conveniently applied to a large number of pressure taps in a wind tunnel model. The unparalleled long-term thermal stability, flexibility and robustness that pressure scanners provide in wind tunnel and flight testing applications, combined with an ability to reconstruct the unsteady components of the measured pressure signals, could enable their use in modern applications involving dynamic flow fields and highly separated flows similar to that considered in this study. Mears et al. [17] provide a comprehensive overview of the flow physics and the fluctuating pressure field around the launch vehicle by utilizing the unsteady pressure measurement technique described in this paper. Here, a brief demonstration of such measurement capability in assessing the flow physics is provided.

Since reference pressure transducers are not available at all 12 port locations, one pressure tap location (Port 10) equipped with a reference transducer has been selected to evaluate the distribution of fluctuating pressure intensity as a function of incoming flow angle ψ_{azm}. This allows for comparing the distributions calculated using the reference transducer with the remote scanner measurements and the reconstructed signal. Case 3 with $h/L = 0.876$, where the vehicle is nearly clear of the launch tower (and the pressure port array is far outside direct influence of the tower), has been selected for this purpose. The fluctuating pressure intensity is calculated by computing the root-mean-square (rms) of each mean-subtracted (pressure fluctuations) time record divided by the dynamic pressure for the test run associated with the ψ_{azm} under consideration. The fluctuating pressure intensities are calculated for each sensor, and results are plotted as a function of the incoming flow angle ψ_{azm} in Figure 17. At $\psi_{azm} = 0°$, port 10 is located at the nominal stagnation point. Note that flow angles from 80° to 100° were not measured due to mechanical constraints of the yaw table. As a result, these angles are greyed out in this figure. Another important consideration in evaluating Figure 17 is the slight difference in the angular location of the reference transducers compared to the scanner measurements. The reference transducers were installed 3° away from corresponding pressure taps. To allow for a more convenient comparison between different distributions, the fluctuating pressure intensity from the reference transducer has been shifted by 3° on the abscissa such that the stagnation points for both sensors are aligned at $\psi_{azm} = 0°$.

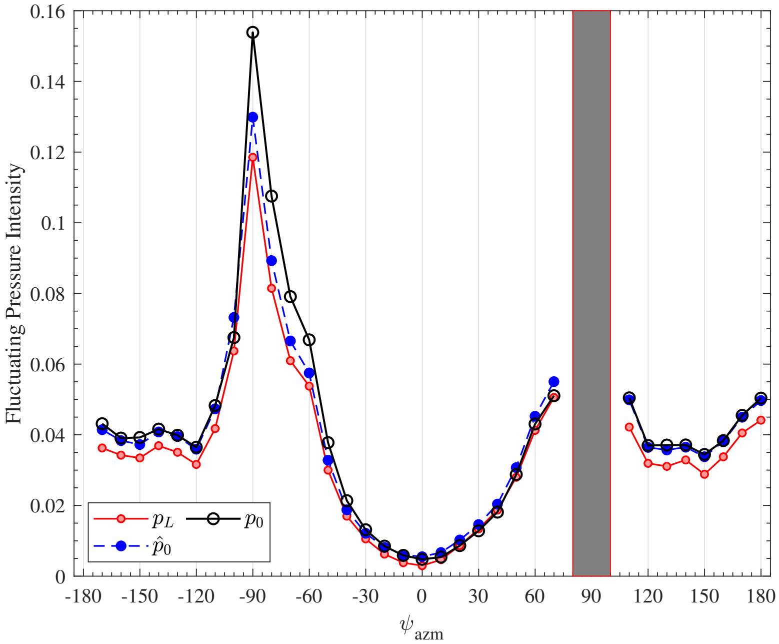

Fig. 17 Fluctuating pressure intensity distribution around the launch vehicle | Case 3: $q_\infty = 50$ psf, $h/L = 0.876$, and $\psi_{azm} = -180°$ to $+180°$

Centered around the stagnation point of the flow at $\psi_{azm} = 0°$, a region of very low pressure fluctuations exists that extends to ±40°. As shown previously, in the regions with insignificant fluctuating pressure content, the agreement between amplitudes of the high-speed reference transducer signal and remote measurements is fairly good. The signal distortion is mainly due to the time delay, and the utilization of the Wiener deconvolution can compensate for the lag. As a result, the difference between fluctuating pressure intensities calculated using the reference and remote sensors is insignificant close to the stagnation point. The fluctuating pressure intensifies smoothly around the launch vehicle from the stagnation point of the flow until it peaks around ±90° close to where flow separation would be expected on the sides of the vehicle. The difference between the reference and remote sensors in the regions with higher fluctuating pressure signals becomes more evident. In these regions, the reconstruction seems to improve the agreement between the rms values. However, the highly unsteady nature of the flow at these locations results in large gradients in the pressure distribution across small angular distances (between the two sensors), making the comparison difficult. Regardless, the overall trends in the intensity distributions are captured quite well. Beyond ±90°, the fluctuating pressure intensity reduces to reach about half the peak amplitude on the rear side of the vehicle where the flow is fully separated. Reaching convergence for the fluctuating pressure intensity in highly separated regions would require longer recordings than those that were achieved in these measurements. However, evaluating the data indicates that at all angular positions, a considerable difference exists between the fluctuating intensities calculated using the reference and remote sensors. In these regions, the flow is separated, and the complex flowfield associated with the wake results in a fluctuating surface pressure signature that can be heavily influenced by amplitude distortions in the tubing between the surface and the remote sensor. The utilization of the Wiener deconvolution results in a significant improvement in the agreement.

V. Summary and Conclusions

This work evaluated the feasibility of using pressure scanning systems for time-resolved pressure measurements in the NASA Langley 14- by 22-Foot Subsonic Tunnel. In the presence of the launch tower, the flow around the forebody shroud of the NASA Space Launch System Block 1B Cargo vehicle resulted in an unsteady pressure field that provides an exceptional validation opportunity for the pressure signal reconstruction methodology discussed in this work. This paper examined three different test cases with highly dynamic surface pressure signatures. These cases were selected to highlight different aspects of the rich flow physics experienced in this experimental campaign. The test article was equipped with a pressure scanner module and five flush-mounted high-speed pressure transducers. Twelve pressure taps were placed around the test article, and each was pneumatically routed to the pressure scanner module. The test article's side-by-side configuration of the pressure taps and high-speed transducers allowed for direct comparison of the reconstructed remotely-measured pressure signals with those of the flush-mounted high-speed transducers. Before the wind tunnel runs, the dynamic response of each length of tubing routed to a port on the pressure scanner was characterized via an in situ tubing response characterization technique. The in situ characterization allowed for identifying and tuning the parameters needed for performing the Wiener deconvolution on the unsteady pressure measurements. During the tests in the wind tunnel, the unsteady pressure fluctuations associated with the flow around the test article were measured. Signals acquired using the pressure scanner module were reconstructed to recover the attenuated and lagged content. The results indicate that both lag and attenuation imposed by the pneumatic tubing can be addressed effectively by utilizing the Weiner deconvolution on the remotely measured signals. This technique can correct the distortion effects and recover the important features in the pressure signal up to approximately 500 Hz.

It was demonstrated that pressure scanners can be effectively utilized for unsteady pressure measurements in wind tunnel applications. In tight areas where mounting a high-speed transducer is impractical, tubing combined with compact pressure scanners can be used along with the compensation methodology described in this paper to provide unsteady pressure measurements. The technique described in this paper also enables current users to recover the unsteady content of the pressure measurements acquired using existing instrumentation. It was observed that the signal-to-noise ratio is critical for improving the quality and extending the range of frequencies that can be reconstructed. Several steps can be taken to improve this parameter. First, the pressure scanner range should be selected to allow maximum sensitivity in a particular testing condition. A careful tubing design can also help with reducing the attenuation effect and improving the signal-to-noise ratio. However, the tubing response can then introduce amplification due to resonance in the dynamics of the tubing system that can also be addressed using the Wiener deconvolution technique. The in situ characterization process is critical in assessing the nature of the tubing system response and extracting the information needed to model the tubing system correctly.

It was also observed that aliasing can become a concern in some applications with signal content at higher frequencies close to the Nyquist frequency. Naturally, increasing the per-port sampling frequency should help with alleviating this issue. However, one must consider the limitations of the scanner's multiplexer and the inaccuracies that can be introduced at high multiplexing rates. These issues are the focus of ongoing investigations. Furthermore, future considerations for validating the technique include application to compressible flows, different test species (such as R-134a refrigerant), and large temperature differences that can be experienced in flight testing or high-speed wind tunnel testing applications. Additional efforts by Resono include uncertainty estimation of the reconstructed pressure signals based on the input parameters required to develop the tubing system response model.

Acknowledgments

This material is based upon work supported by the National Aeronautics and Space Administration through Space Act Agreement 34369 with the University of Wyoming. We gratefully acknowledge the assistance of the 14- by 22-Foot Subsonic Tunnel facility staff in conducting these experiments.

References

[1] Whitmore, S., Wilson, M., and Eilers, S., "A Novel Technique for Reconstructing High-Frequency Transient Rocket Chamber Pressure Measurements," *45th AIAA\ASME\SAE\ASEE Joint Propulsion Conference & Exhibit*, 2009.

[2] Elliott, S., Lax, P., and Leonov, S. B., "Control of Shock Positions in a Supersonic Duct by Plasma Array," *AIAA SCITECH 2022 Forum*, American Institute of Aeronautics and Astronautics, 2022.

[3] Stephen, E. J., Hoenisch, S. R., Riggs, C. J., Waddel, M. L., Bolender, M. A., and McLaughlin, T. E., "HIFiRE-6 Unstart Conditions at Off-Design Mach Numbers," *53rd AIAA Aerospace Sciences Meeting*, American Institute of Aeronautics and Astronautics, 2015.

[4] Whitmore, S. A., Lindsey, W. T., Curry, R. E., and Gilyard, G. B., "Experimental characterization of the effects of pneumatic tubing on unsteady pressure measurements," Tech. rep., National Aeronautics and Space Administration, 1990.

[5] Rivers, N. A., van Dam, C. P., Brown, P. W., and Rivers, R. A., "Flight Investigation of the Effects of Pressure-Belt Tubing Size on Measured Pressure Distributions," Tech. rep., National Aeronautics and Space Administration, 2001.

[6] Wu, G., Zhang, L., and Yang, K., "Development and Validation of Aerodynamic Measurement on a Horizontal Axis Wind Turbine in the Field," *Applied Sciences*, Vol. 9, No. 3, 2019, p. 482.

[7] Xiao, H., Ou, C., Ji, H., He, Z., Liu, N., and Yuan, X., "Low-Cost and Aerodynamics-Aim Hypersonic Flight Experiment MF-1," *MATEC Web of Conferences*, Vol. 316, 2020, p. 04006.

[8] Ganesan, S., pauriyal, R. C., Thiyagarajan, R., and Khan, P. A. K. M., "Aerodynamic Performance Assessment on Typical SUV Car Model by On-Road Surface Pressure Mapping Method," *SAE Technical Paper Series*, SAE International, 2021.

[9] Bergh, H., and Tijdeman, H., "Theoretical and experimental results for the dynamic response of pressure measuring systems." TR F.238, Amsterdam Nationaal Luchtvaarlaboratorium (National Aeronautical and Astronautical Research Institute), 1965.

[10] Nikoueeyan, P., Hind, M. D., Strike, J., Singh, M., Naughton, J. W., Keeter, S., and Dahland, M., "Characterization of Unsteady Pressures on a Blunt Trailing Edge Using a Direct-Mount Pressure Scanner," *AIAA Aerospace Sciences Meeting*, American Institute of Aeronautics and Astronautics, 2019.

[11] Whitmore, S. A., and Wilson, M. D., "Wiener Deconvolution for Reconstruction of Pneumatically Attenuated Pressure Signals," *AIAA*, Vol. 49, 2011, pp. 890–897.

[12] Strike, J. A., Hind, M. D., Saini, M. S., Naughton, J. W., Wilson, M. D., and Whitmore, S. A., "Unsteady Surface Pressure Reconstruction on an Oscilating Airfoil Using the Wiener Deconvolution Method," *27th AIAA Aerodynamic Measurement Technology and Ground Testing Conference*, American Institute of Aeronautics and Astronautics, 2010.

[13] Pinier, J. T., Herron, A., and Gomez, R. J., "Advances in the Characterization of NASA's Space Launch System Aerodynamic Environments," *AIAA Aviation 2019 Forum*, American Institute of Aeronautics and Astronautics, 2019.

[14] Chan, D. T., Paulson, J. W., Shea, P., Toro, K., Parker, P. A., and Commo, S. A., "Aerodynamic Characterization and Improved Testing Methods for the Space Launch System Liftoff and Transition Environment," *AIAA Aviation 2019 Forum*, American Institute of Aeronautics and Astronautics, 2019.

[15] Ratnayake, N. A., Krist, S. E., Ghaffari, F., and Deere, K. A., "Computational Fluid Dynamics Methods Used in the Development of the Space Launch System Liftoff and Transition Lineloads Databases," *AIAA Aviation 2019 Forum*, American Institute of Aeronautics and Astronautics, 2019.

[16] Krist, S. E., Ratnayake, N. A., and Ghaffari, F., "Kestrel Results at Liftoff Conditions for a Space Launch System Configuration in Proximity to the Launch Tower," *AIAA Scitech 2019 Forum*, American Institute of Aeronautics and Astronautics, 2019.

[17] Mears, L. J., Shea, P. R., Collins, J. G., Walker, M. A., Langston, S. L., Pinier, J. T., Nikoueeyan, P., Perry, M., Strike, J., Wimpenny, B., Hind, M., and Naughton, J. W., "Unsteady Pressure Acquisition on the 1.75% Scale SLS Block 1B Cargo Liftoff Configuration," NASA TM 20220002633, National Aeronautics and Space Administration, 2022.

[18] Mears, L. J., Shea, P. R., Collins, J. G., Walker, M. A., Pinier, J. T., Nikoueeyan, P., Perry, M., Strike, J., Wimpenny, B., Hind, M. D., and Naughton, J. W., "Unsteady Surface Pressures on the Space Launch System Block 1B Cargo Liftoff Configuration," *AIAA Aviation 2022 Forum*, American Institute of Aeronautics and Astronautics, 2022.

[19] Tijdeman, H., "Investigation of the Transonic Flow Around Oscillating Airfoils," NLR-TR 77090U, Amsterdam Nationaal Luchtvaarlaboratorium (National Aeronautical and Astronautical Research Institute), 1977.

[20] Gentry, G. L., Frank Quinto, P., Gatlin, G. M., and Applin, Z. T., "The Langley 14-by 22-Foot Subsonic Tunnel: Description, Flow Characteristics, and Guide for Users," Nasa-tp-3008, National Aeronautics and Space Administration, 1990 1990.